Steady and Unsteady Numerical Characterization of the Stable Operating Range of a Highly-Loaded Low-Pressure Compressor Stage

Riccardo Toracchio

Turbomachinery and Propulsion Department, von Karman Institute for Fluid Dynamics, Belgium, riccardo.toracchio@vki.ac.be

Supervisor: Fabrizio Fontaneto

Associate Professor, Turbomachinery and Propulsion Department, von Karman Institute for Fluid Dynamics, Belgium, fontaneto@vki.ac.be

University Supervisor: Koen Hillewaert

Associate Professor, Aerospace and Mechanical Engineering Department, University of Liège, Belgium, koen.hillewaert@uliege.be

Abstract

Despite the improved propulsive performance induced by short-inlet and Boundary-Layer-Ingestion (BLI) aircraft architectures, the engine is forced to operate with non-homogeneous inlet flows. The low-pressure compressor is therefore subjected to the effects of the incoming distorted inlet flow at the outlet of the fan that can significantly affect its performance and stability. Before any characterization and description of the flow topology and performance is carried out under the effect of the distortion, clean conditions need to be analysed to allow a proper comparison with the distorted case and the available experimental results. On this purpose, steady and unsteady Reynolds-Averaged-Navier-Stokes (RANS) simulations of the VKI DREAM low-pressure compressor stage are performed.

Keywords: Distortion, CFD, unsteady, compressors

1. Introduction

Advanced aircraft technologies are currently in the focus of research to address the environmental goal of reducing aircraft emissions within the next decade and beyond [1]. Short-nacelle geared high bypass turbofans and BLI engines are among the most promising technologies to improve fuel and propulsive efficiency in the short and long term respectively, forcing nevertheless the engine to operate with a highly distorted inlet flow [2][3]. Although operability and performance deterioration of fans under distorted conditions has been the primary focus of research in last decades [4][5][6], given its strong impact in the definition of the overall propulsive efficiency, almost no information is currently available on the low pressure compressor (booster), despite its crucial role in the forthcoming generation of engines. The complex flow distortion pattern observed behind the fan will indeed influence the underlying physical mechanisms taking place within the compressor stage, possibly jeopar-

dizing performance and stability of the whole engine. Due to the impossibility of extending the results obtained for fans to the low-pressure compressor as a consequence of the marked aerodynamic and structural design differences, this research project aims at providing a complete characterization of the physical phenomena driving loss generation and stability deterioration in modern Low-Pressure Compressors (LPC) when distorted flow conditions set up.

However, before any investigation is carried out to understand the effects of inlet non-uniformities on the LPC, its characterization in clean conditions is needed in order to highlight the differences between the baseline and distorted configuration, and to add meaningful information to the available experimental results. To reach this goal, steady and unsteady RANS simulations are run on the highly-loaded low-pressure VKI DREAM compressor stage, which is representative of the first stage of a modern geared turbofan booster. The aim is to provide an overall assessment of the global performance of the machine, highlighting flow

mechanisms driving the loss generation.

In the first part of the paper the final configuration of the numerical domain and mesh are described, along with the numerical setup employed. In the second part, the results of the steady and unsteady simulations at design conditions are provided.

2. Test section and instrumentation

The test section considered in this work as reference to run the numerical simulations is the DREAM compressor stage. It is installed in the VKI R4 closed-loop high-speed test-rig, composed by a tank used as settling chamber (1), the test section (2), a discharging collector at the compressor outlet (3), a return channel to guide the air back to the reservoir (4), and a throttling valve to run the compressor at different operating conditions (5) (Figure 1). The tank is equipped with air/water heat exchanger to allow a temperature control at the test section inlet with an accuracy of +/-1K. The temperature control and the closed-loop architecture allow an independent variation of Reynolds and Mach numbers, giving the chance to test in representative cruise and take-off aircraft conditions. The rotor is driven by a 450 kW DC motor with a continuous control of the rotational speed, and it is coupled to a 12:1 gearbox that increases the rotor speed up to 9000 RPM.
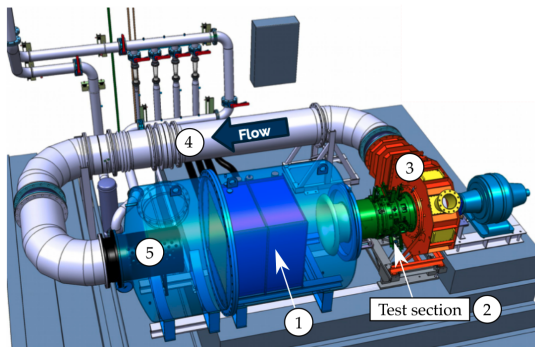

Figure 1: VKI-R4 closed-loop high-speed compressor rig.

The test section is a 1.5 stage characterized by 100 inlet guide vanes, to simulate the radial distribution of flow angle behind the fan, followed by 76 rotor blades and 100 stator blades. A smooth convergent bell-mouth guides the flow from the reservoir to the test section. Figure 2 shows a sectional view of the presented test section.

Total pressure, temperature, Mach number and flow angles are measured at four axial locations corre-
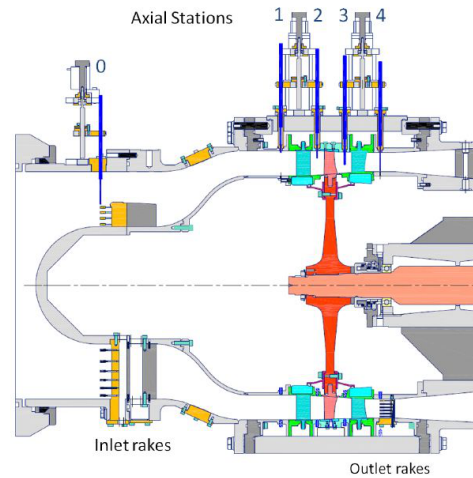

Figure 2: DREAM test section.

sponding to the stage inlet (plane 1), IGV outlet (plane 2), rotor outlet (plane 3) and stage outlet (plane 4). Each axial locations allows four circumferential positions of the instrumentation at 0, 90, 180 and 270 degrees, and a span-wise variation of the probe location. Moreover, to avoid leaks for the presence of grooves, a circumferential traverse mechanisms has been realized by rotating the stators instead of the probes. In plane 0, located upstream of plane 1, and in plane 4, 4 rakes are distributed circumferentially to compute the global performance. Every rake is composed by 6 Kiel heads, equipped with a pressure tap and a T-type thermocouple junction, to provide a proper area-averaging of total quantities. The performance map for the compressor is obtained by sistematically closing the throttling valve while keeping constant the corrected rotational speed of the compressor. A good approximation of the mass-flow is possible by the only 6 inlet rakes. Moreover, at every measurement location, static pressure is acquired trough 5 static pressure holes at casing and other 5 in the hub walls distributed along the circumference . The static pressure along the span is retrieved by linear interpolation of the mean static pressure at hub and shroud. A pitot tube is traversed in plane 0 to assess the linearity of the radial distribution of the static pressure. To compute the efficiency and performance maps of the compressor, data have been acquired with a frequency of 2 Hz. The uncertainty associated to the measurements is calculated with the ASME method [7] and the values are presented in a 95% confidence interval. The uncertainty values are +/- 0.5 mbar and +/- 0.7K, resulting in a +/- 0.00053 uncertainty value for the pressure

ratio.

For the unsteady instrumentation, 15 measurement points have been located at the casing for time-resolved static pressure measurements. These sensors have a resonance frequency higher than 200kHz, but the bandwidth is limited to 60 kHz due the metallic insert where they are contained. The sensors cover an arc of 42°, are equally spaced in one rotor pitch, and are axially displaced between plane 2 and 3. The static pressure at the hub is retrieved in plane 3 and 4 by using sensors located at 66°. Moreover, they are characterized by an uncertainty of +/- 1.2 mbar, again computed with the ASME method [7]. As last, a fast-response pressure probe, characterized by a resonance frequency of around 300 kHz and uncertainty calibration of +/- 1.8 mbar, is located at mid-span of the rotor outlet at 90°. The acquisition of the time-resolved data is carried out at a frequency of 1MHz for 10 s.

3. Numerical domain and setup

The numerical domain and setup employed in the simulations was chosen to provide as high as possible level of accuracy with respect to the experimental results, while keeping a limited computational cost. Hereafter a description of the procedure followed to assess the quality of the domain, mesh and numerical setup is presented.

3.1. Numerical domain

The numerical domain shown in Figure 3 is representative of the real geometry of the DREAM test section between Plane 1 (IGV inlet) and 4 (Outlet stage). The outlet section is imposed downstream of plane 4 to avoid any possible influence of the outlet boundary condition on the measurement plane.
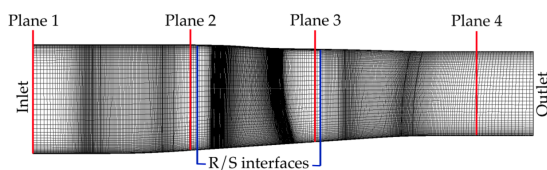

Figure 3: Numerical domain.

The process for the definition of the numerical domain went through the identification of real geometrical features playing a role in the assessment of global performance and flow field of the machine, which in this case are: fillets, tip gaps, hot geometries and cavities. Because of their significant impact on the definition of secondary flow structures at hub and casing

respectively [8][9], along with the limited increase in mesh size determined, fillets and tip gaps have been directly implemented considering their averaged measured value. Hot geometries were also considered to take into account possible deformations of the machine when operating.

However, as highlighted by Babin et al. in [10] cavities can play an important role if looking to the performance of the machine and to the state of the boundary-layer at the rotor leading-edge. This can influence the axial component of the velocity and therefore the incidence at low span, forcing the flow to separate on the hub suction side wall. At the same time, the presence of cavities in the numerical domain impacts considerably the computational cost, especially if unsteady RANS have to be performed. A study on the impact of rotor cavities was therefore undertaken to assess the quality of the results against the increased mesh size. Matching connections are used at the interface between cavities and main channel to allow an improved numerical accuracy of the leakage flow exchanged with the cavity. The same mesh topology was kept in both configurations to avoid any possible grid-dependent modification of the flow field (Figure 4), bringing the mesh size to reach 9.6 and 7.4 million cells for one passage in the cavity and no-cavity case respectively. The ratio between the grid points in the cavities and the rotor domain was chosen to be as close as possible to one to allow an improved balance of the solution quality in the two regions.
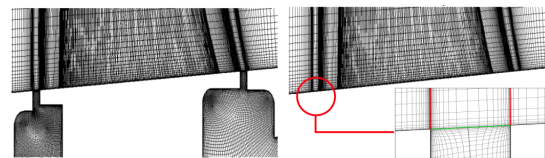

Figure 4: Mesh topology employed to study the effect of the cavity.

The comparison is hereafter presented in terms of global performance and rotor outlet total pressure difference, which is explicative of the losses generated at low span. The flow field over the outlet stator was not significantly affected by the presence of the cavities. As highlighted in Figure 5 a reduction of performance occurs when cavities are considered, and this is mainly due to the variation of flow topology at low span due to the interaction with the cavity, as highlighted in Figure 6. A value of the mass flow equal to 1 is representative of the outlet boundary condition which in this case was imposed equal to the experimental value. The averaged value of total pres-

sure for span lower than 30% is reduced by the flow ejected from the cavity (Figure 6, point 1), and the flow exchanged at the interface increases locally the incidence due to blockage effects, affecting size and intensity of the hub corner separation (Figure 6, point 2). Red regions are instead representative of low total pressure regions of the no-cavity configuration. The high values encountered on the hub wall at 0.25 and 1.25 were thought to be generated by the presence of a passage vortex, but no clear evidence of its presence can be detected from the experiments and the CFD simulations.
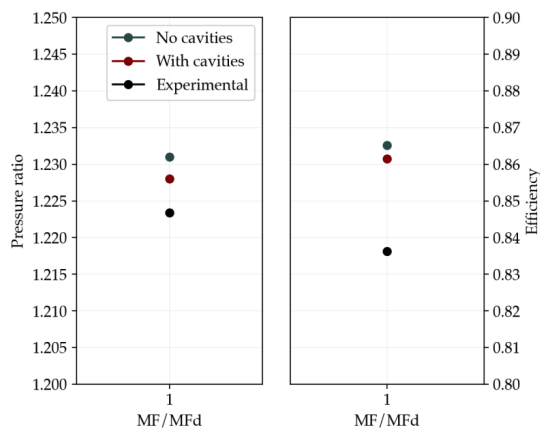

Figure 5: Comparison of cavity, no cavity case and experimental global performance.
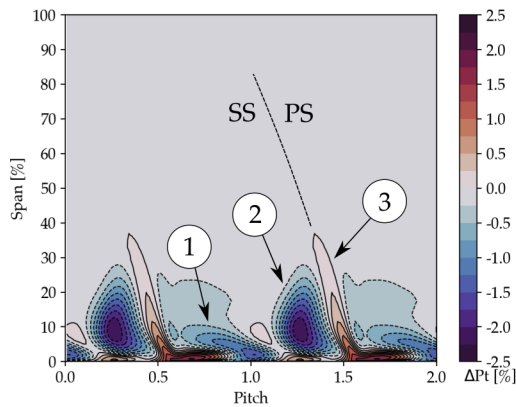

Figure 6: Difference of total pressure maps at rotor outlet between cavity and no cavity case.

As overall conclusion, despite the significative difference of the RANS simulations with respect to the experiments, the presence of the cavity does not seem to impact strongly the characterization of the global

performance and flow field of the compressor, keeping the difference always limited to maximum 2.5%. Therefore, given the advantage of a reduced mesh size, the no-cavity configuration was selected for the steady and unsteady characterization of the machine.

3.2. Mesh and grid refinement study

For a better control of the grid quality, multi-block structured mesh was implemented with Autogrid5 and IGG softwares. An O4H symmetric blade-to-blade topology was considered for every blade row, and matching conditions were applied on the periodic boundaries. OH topology was used instead for the rotor tip gap region, with a number of cells equal to 30% of the rotor in the span-wise direction and 20% constant size cells in the mid-flow gap region. The B2B section offset method was selected for the geometry creation of the hub and shroud fillets. 20 span-wise points were used, along with a minimum angle of 25° to allow a good angular deviation and distribution of points on the wall. Mesh quality assessments showed minimum skewness level, maximum aspect and expansion ratio of the cells of 22°, 2000 and 2.5 respectively, which are considered to provide good quality results. Expansion ratio and cell width at the wall were selected to guaranty uniform variation of the cells from the wall and a good interface with the main flow, allowing everywhere a value of the y+ lower than 3. Moreover, only for the present grid refinement study, radial equilibrium imposed on the static pressure was selected as outlet boundary condition.

A generalized Richardson extrapolation approach [11] [12] was adopted to quantify the uncertainty introduced by spatial discretization on the flow quantity of interest. At such extent, three mesh levels were considered with 0.64 (coarse), 5.12 (medium) and 40.96 (fine) million cells respectively, obtained from an isotropic refinement in the θ, R and Z directions by a factor of 2 (size ratio of 8 among the grid levels). The comparison is here proposed in terms of global performance (total pressure ratio and efficiency, Figure 7) and percentage difference of rotor outlet total pressure maps of the coarse, medium and fine solution with respect to the 2D Richardson extrapolation computed on the same plane (Figure 8).

No significant difference is present between medium and fine solutions for both global performance and rotor outlet maps, while the coarse solution shows discrepancies larger than 5% and 12% respectively when compared to the Richardson extrapolation. The latter is highlighted mainly in the shape
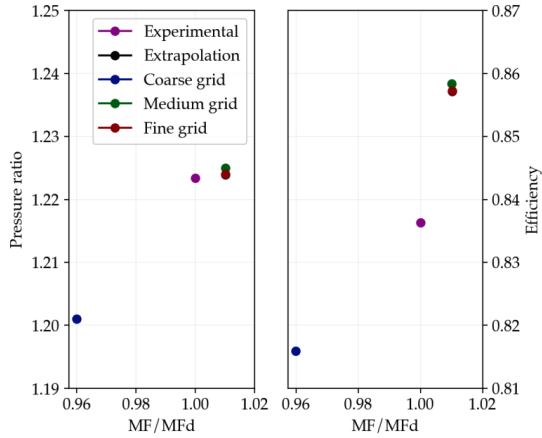
Figure 7: Comparison between mesh levels on the compressor and efficiency maps.
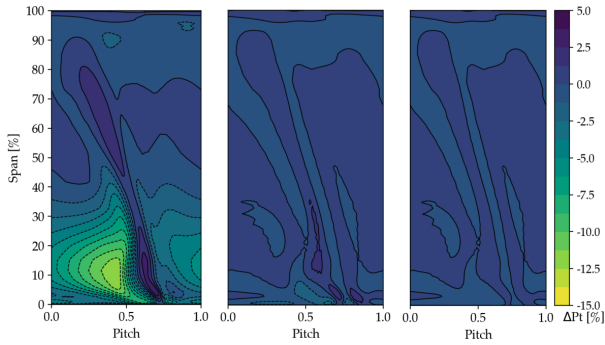

Figure 8: Comparison of the mesh levels with respect to the Richardson extrapolation.

and amplitude of the hub corner separated region, as shown in yellow in Figure 8. The increased numerical dissipation induced by the low refinement level of the coarse mesh can indeed influence the solution in the regions strongly affected by secondary-flows and losses, over-predicting the reduction of the total pressure. Moreover, the extrapolated point in the global performance map almost overlap the one computed from the fine mesh, becoming therefore not visible in the figure.

As a conclusion of the grid refinement procedure, given the good level of accuracy provided by the medium mesh when compared to the reduced computational cost with respect to the fine mesh, it was selected as best candidate to employ in the simulations.

3.3. Numerical setup

Numeca FineTurbo software was used to solve the fully-turbulent compressible Reynolds-Averaged-Navier-Stokes equations, spatially discretized with a cell-centered finite volume formulation on a multi-block structured grid. The eddy viscosity assumption was used to account for turbulent effects, and the two equations k-ω SST model was considered for the turbulence closure as consequence of the accuracy provided in both near-wall and free-stream regions. Inlet total pressure and temperature boundary conditions were imposed equal to the experimental pitch-average span-wise distributions, and the same was done for the mass-flow boundary condition imposed at the outlet. The outlet static pressure based on the radial equilibrium was used only in view of the simulations performed for the grid refinement study, but it appeared to be a very unstable boundary condition for the present case, forcing the machine to develop open hub corner separations which are not in line with experiments. Moreover, air was considered as a calorically perfect gas, and the walls of the numerical domain as adiabatic. Time integration to a steady-state solution was achieved with an explicit Runge-Kutta method combined with an implicit residual smoothing approach, while considering time discretization based on local and dual time stepping techniques for the steady and unsteady problem respectively.

For the steady computations a full non-matching mixing plane approach was used at the rotor/stator interfaces showed in Figure 3, while for the unsteady simulations a domain scaling approach was considered. The latter is based on the constraint that the pitch distance must be identical on both sides of the rotor/stator interface, implying either to increase the number of modelled passages or to scale the geometry accordingly. In the present study, the number of rotor passages was supposed to be 75 instead of 76, to allow therefore the applicability of the domain scaling approach by implementing only 4/3/4 passages for the IGV, rotor and outlet stator respectively. A preliminary evaluation of the span-wise diffusion factor computed in the case of 75 rotor blades confirmed that no significant variation with the respect to the original geometry should be expected. Moreover, the error in the computation of all time frequencies can be considered negligible being the scaling coefficient very close to 1. Moreover, the application of the explicit Runge-Kutta scheme on a sine wave confirmed that at least 30 points are required for a proper representation of every harmonic of interest. The experimental evidence of the appearance of physical phenomena with a frequency four time larger than the rotor Blade Passing Frequency (BPF) suggested the application of 120 time steps per passage. As last point, the unsteady computation was initialized with a steady simulation

employing frozen rotor approach at the domain interfaces.

4. Results

The main idea behind the characterization of DREAM in clean conditions was to provide a comparison against the available experimental results in the same operating conditions, and to further describe the most relevant flow phenomena taking place in the machine. The description of the global performance was already presented in the first part of the paper, therefore here an initial assessment, by means of low order models applied to which appeared to be the highest source of losses in the machine is proposed, followed by the description of the span-wise distribution of flow quantities retrieved by the steady simulations. To conclude, the full 3D characterization of the flow by means of the unsteady simulations is presented.

In view of the comparison with the distorted case, design conditions at 100% speed were considered for this analysis. Despite the large value of efficiency, this operating point is considered one of the most interesting for the assessment of the distortion effects being representative of cruise aircraft conditions. Moreover, the limited variation of incidence and mass-flow allowed at high speed make this a critical operating point for the compressor under inlet distortions.

4.1. Low-order modeling

The stall indicator and the diffusion factor coefficients defined by Lei [13] were employed as a preliminary approach to quantify the extent of the reversed flow in the hub region and the diffusion limit conditions with respect to corner stall. Figure 9 shows the span-wise distribution of the diffusion factor in the rotor blade passage, which presents a closed corner structure for span values lower than 30%, as highlighted by the CFD simulations.

The diffusion factor is mainly affected by blade and incidence angles which are representative of the overall pressure rise, by the turning in the end-wall region (cross-flow) and solidity, that again influences the pressure gradient developed over the suction side of the blade. In the present case, the large blade turning at low-span combined with a local increase of the flow incidence at the rotor leading edge due to the high speed of the rotating platform appeared to be at the base of such high value of this parameter. Large values of the diffusion factor are present all over the blade height, determining a span-wise averaged value
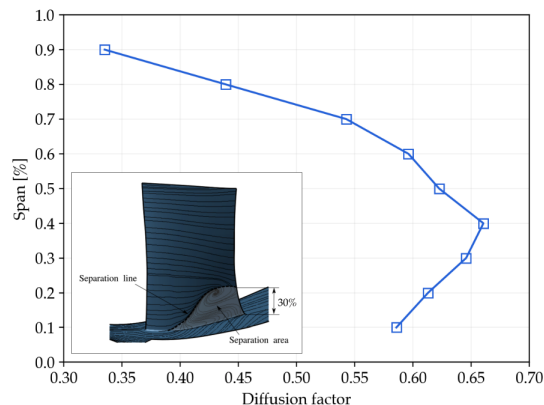

Figure 9: Span-wise diffusion factor distribution on the rotor blade.

of 0.56. The reduction visible in the tip region is mainly due to the low blade turning compared to low-span regions, still keeping values larger than 0.3. The maximum value is reached at 40% span being this location at the limit of the hub separation span-wise extent.

Figure 10 presents instead the position of the DREAM test section compared to the results provided by Lei [13]. The diffusion factor is here presented in terms of span-wise averaged value, while the stall indicator, representative of the blade loading reduction with respect to conditions outside of the separated region, is referred to mid-span, where the largest values of the diffusion factor appear. On this graph, DREAM is located in the region that exhibits open corner separations but lays almost on the line prolongation representative of closed separations, which is a condition not considered in the Lei's study. This situation could explain the experimentally and numerically evident presence of a closed separation, being nevertheless at limit of hub corner stall.

The corner shape factor criterion [14] was considered to further characterise the corner separation and its proximity to instability. This parameter is defined as the angle between co- (V1) and reversed flow vector (V2) identified on the peak streamline curvature, as highlighted in Figure 11, and can change between 0 and π, where the latter represents the limit condition to the hub stall. In the present case this angle reaches 162°, again confirming the tendency of DREAM to exhibit severe hub corner separations.

Finally, Bennington [15] derived a simple model to quantify the location and movement of the mean flow/tip leakage interface as a consequence of the momentum balance between the approaching flow and
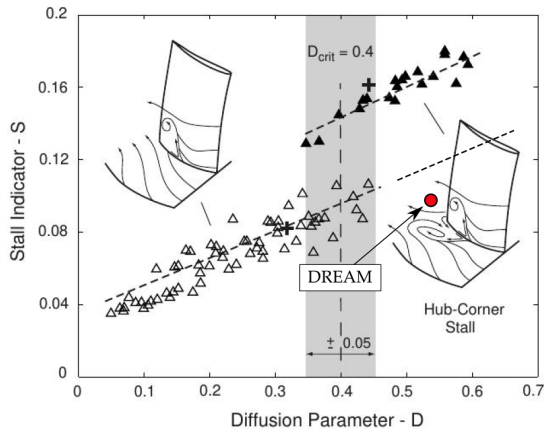
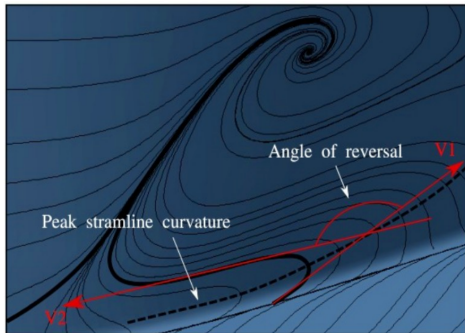Figure 10: Location of the DREAM test section in the Lei's diagram.

Figure 11: Angle of reversal in the DREAM stage.

Figure 12: CFD at casing versus Bennington prediction.

the tip gap reverse flow, and it is here proposed as a comparison with respect to steady RANS simulations (Figure 12). The interface distance with respect to the blade surface was computed on a blade location referred to the near-stall conditions. In the same figure a very good agreement is shown between CFD and model prediction.

4.2. Span-wise distributions

Pitch-wise mass averaged distributions are retrieved from the steady state simulations performed on the compressor and are hereafter shown for total pressure, temperature and flow angles respectively at plane 3 (rotor outlet) and 4 (stator outlet).

The total pressure was selected to identify the largest source of losses in the blade passage (Figure 13). In plane 3 two are the highest regions of discrepancy with respect to the experimental results, and these are the end wall regions. On the hub, the CFD over-predicts the reduction of total pressure induced by the hub corner separation, while on the tip region
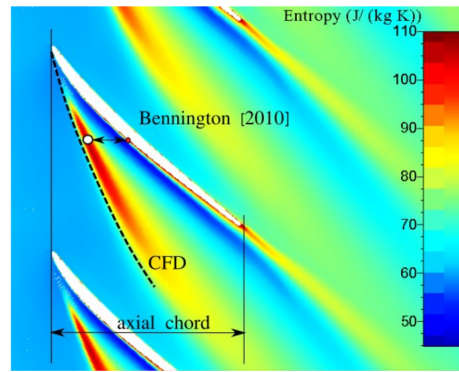
the opposite trend is visible. This will be shown also later in the outlet maps: the span-wise extent of the tip leakage flow is not clearly visible from the CFD, while it appears to have a strong impact on the experiments. The abrupt variation of total pressure at very low span for the experiments is the result of the cavity leakage flow which is not present in this configuration of the CFD domain. Less differences are instead visible from the total pressure distribution at plane 4. The total pressure losses in the experiments increase indeed with respect to the CFD for span lower than 50% and the flow tends to homogenise. Close to the tip region, again smaller value of the experimental total pressure are presents if compared to CFD. However, the reduction of total pressure visible at 70% is due to the span-wise propagation of the tip leakage flow coming from the rotor. General differences in the mid-span region between experiments and CFD could be addressed to a not perfect matching of the operating point in the two cases. The experimental uncertainty on the total pressure is too small to be visible from the figures. However, despite the difference in the end-wall regions, to results of the CFD simulations are considered in good agreement with experiments.

The most evident difference in the span-wise distribution of total temperature (Figure 14) is the mismatch in the tip region between CFD and experiments. The heat transfer through the casing walls of the facility from the external laboratory environment indeed impacts the value of total temperature, and therefore efficiency, at high span. This does not appear in the computations since adiabatic wall boundary conditions were employed. However, for most of the span height the CFD is within the experimental uncertainty, defining therefore good overall matching between the different distributions.

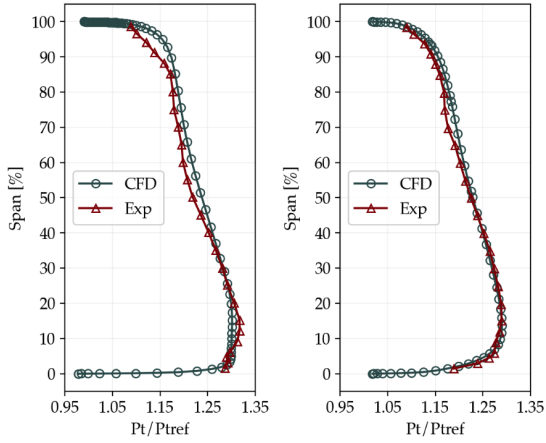Figures 15 shows respectively the distribution of

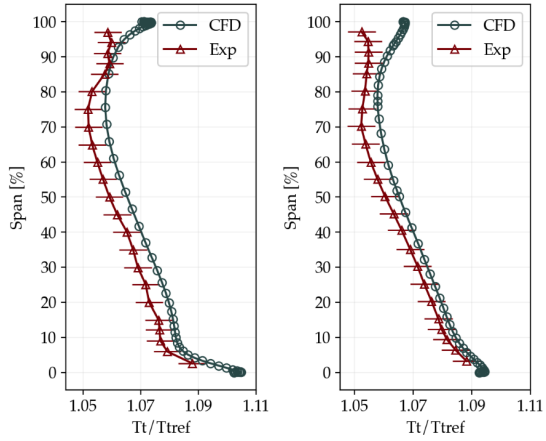Figure 13: Total pressure span-wise distribution at rotor outlet (a) and stator outlet (b).

Figure 14: Total temperature span-wise distribution at rotor outlet (a) and stator outlet (b).

the flow angles (relative (a) and absolute (b)) and entropy at rotor outlet and stage outlet planes. The distribution of the relative flow angle in plane 3 is mainly determined by the outlet blade angle which increases with respect to the axial direction moving to higher span. It is worth to notice the local reduction for span lower than 10%. This effect is associated to a cross-flow motion into the blade passage. The flow indeed, after entering the rotating platform increases at very low span the incidence level, with subsequent generation of a sonic pocket due to the large values of relative velocity. However, after 20% of the chord, the flow that initially moved far from the blade starts to migrate toward the suction side on the second half of the blade, to arrive in plane 3 with reduced value of the relative flow angle. The span-wise variation of the

flow angle in plane 4 is instead in the range -6°, +2° the majority of which occurs into the boundary layer. For the rest of the span (10%-90% range) the variation of the absolute angle is kept lower than 1.5°. For this case, no comparison is provided with respect to the experimental results.
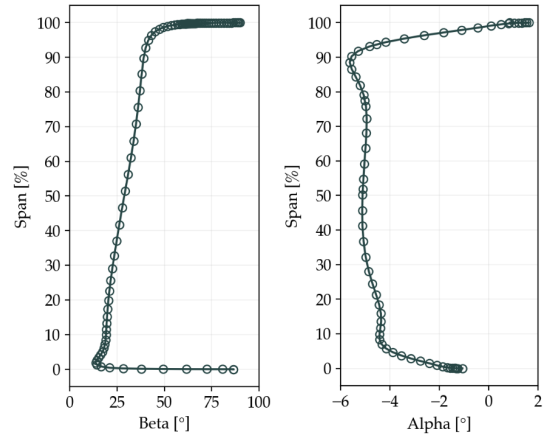

Figure 15: Flow angle span-wise distribution at rotor outlet (a) and stator outlet (b).

4.3. Detail flow characterization
4.3.1. Rotor outlet maps

Figures 16 and 17 show the total pressure distribution and the corresponding RMS computed from the flow fluctuations with respect to the Phase-Lock-Averaged (PLA) value at the rotor outlet plane, allowing the description of the flow field and distinguish the unsteady flow structures appearing in the blade passage. Since plane 3 (rotor outlet) belongs to the rotating frame of reference in the numerical domain, the PLA was computed to detect and isolate the fluctuations synchronous to the IGV/stator Blade-Passing-Frequency (BPF). The total pressure map highlights a general reduction of the total pressure in the rotor wake, with a thickening under 30% span due to the presence of the hub corner separation. This is clearly visible also from the RMS distribution, where a peak, reached in the same location, highlights that the hub corner separation represents one of the highest source of unsteadiness in the blade passage. Large values of RMS are also visible on the pressure side at low span. However, no clear secondary structure appears from the analysis of the flow in that region, meaning that rotor/stator interactions may be at the base of such fluctuations.

To provide a comparison with respect to the experimental results, the percentage difference between
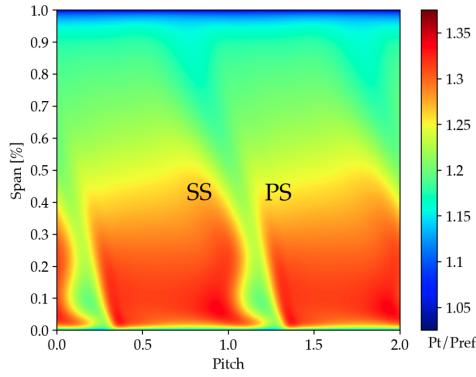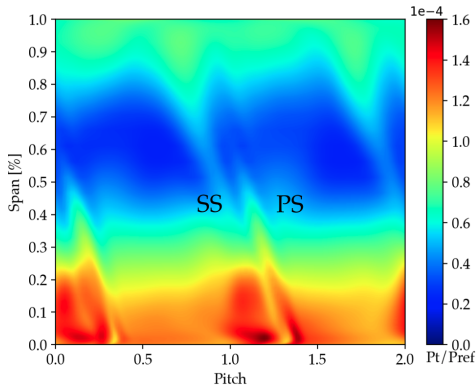
Figure 16: Total pressure map at rotor outlet.

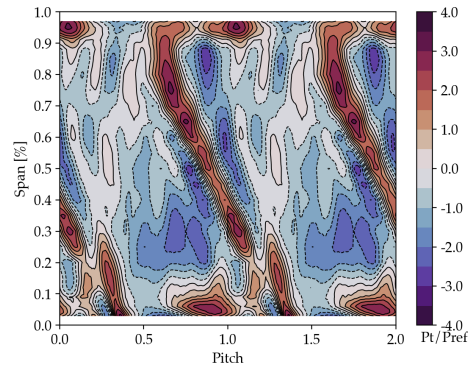Figure 17: Total pressure RMS map at rotor outlet.

CFD and experimental total pressure maps are shown in Figure 18. The CFD over-predicts the total pressure level in the wake and in the hub corner region. Moreover, the intensity of the tip clearance flow is highly under-predicted in the CFD, and this is the reason why the structure of this vortex does not appear clearly on the outlet plane. This can not be linked with any issue of the mesh in the tip clearance, being the grid resolution in that region very high. Again, the high total pressure region at low span on the pressure side of the blade is visible.

The experimental and numerical RMS maps are not compared given the large difference in fluctuation amplitudes. Experimental signals contain indeed turbulence fluctuations which are not taken into account in unsteady RANS simulations, where only the statistical content of the fluctuations linked to the domain periodicity is visible.

4.3.2. Casing maps

Results are hereafter shown in terms of entropy distribution at casing. Entropy was selected as the quan-

Figure 18: CFD vs experiments at rotor outlet.

tity of interest given its capability to spot more in detail the unsteady features of the flow with respect to the static pressure.
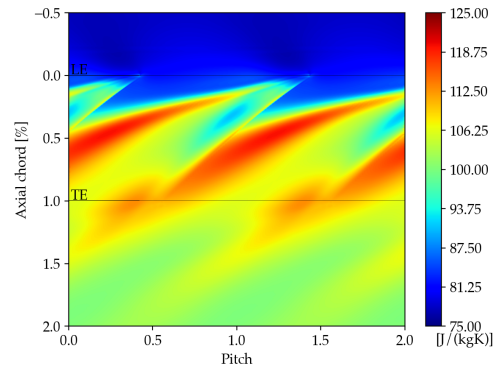

Figure 19: Entropy distribution at casing.

The entropy distribution at 100% span (Figure 19) shows an interface between mean flow and tip leakage flow inclined of almost 20° with respect to the line connecting two adjacent leading edges. The central core of the tip leakage is highlighted by a large value of the entropy and impacts on the pressure side of the adjacent blade from half of the axial chord until the trailing edge. An investigation of the instantaneous entropy pattern highlights that the tip leakage flow enters indeed the passage of the adjacent blade only in the second part of the blade, generating an high entropy region on the suction side trailing edge of the next blade. The flow is fully governed by the IGV wake which estabilish an oscillation of the entire structure of the tip leakage flow. The RMS highlights clearly a large value of the fluctuations at the interface
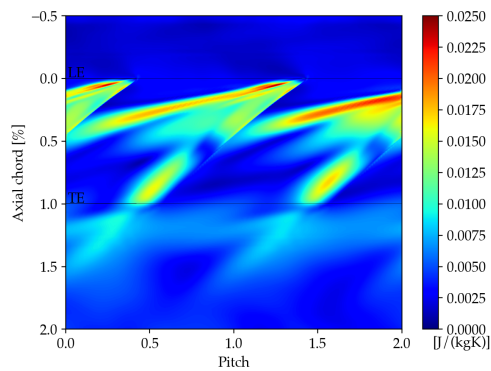
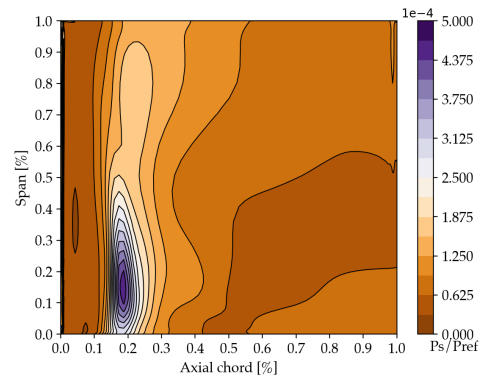Figure 20: Entropy RMS distribution at casing.

Figure 22: Static pressure RMS distribution over the suction side blade surface.

with the meanflow, while high peaks can be found also over the suction side of the blade.

4.3.3. Blade suction side

Also in this case, the unsteady behavior of the blade is shown in terms of static pressure and RMS distributions over the suction side of the blade as presented in Figures 21 and 22. The former shows the clear presence of a shock developing all along the span, which is mainly due to the high relative velocity reached by the flow just after the blade leading edge. The plateau of static pressure visible at span lower than 30%, in the downstream part of the blade (after 40% axial chord) is the clear presence of the hub corner separations, which is further confirmed by the high value of the RMS in the same region. Moreover, the largest source of unsteadiness on the suction side of the blade comes from the fluctuations of the supersonic pocket.
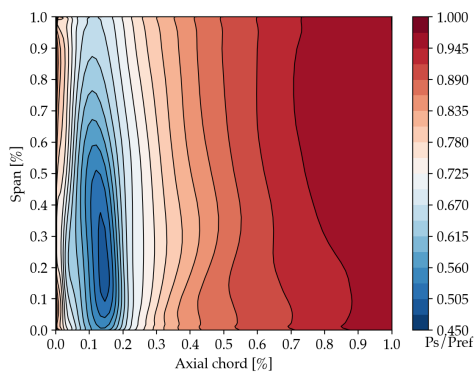

Figure 21: Static pressure distribution over the suction side blade surface.

5. Conclusion

Inlet distortions can considerably impact the performance and stability of a machine, altering localized regions of the flow field. The presented paper had the target to identify and characterize the most critical physical phenomena in a low-pressure compressor running in clean conditions to allow a proper assessment and quantification of the effects induced by the distortion. The provided numerical results showed good agreement with the experiments, and highlighted the presence of two main phenomena of interest: hub corner separations and tip leakage flows. The available literature confirms indeed that these are typical phenomena in axial compressors affected by the presence of the distortion.

The analysis of the numerical domain allowed to conclude that fillets and tip gaps should always be taken into account given their limited impact on the mesh size, while it is not worth in the present case to consider the presence of cavities due to the very small improvement of numerical results at the expense of a large increase of the computational cost.

Despite the over-prediction of the total pressure reduction in the separated region, the numerical results showed a span-wise extent of the rotor corner separation equal to 30% of the overall blade height and that it represents one of the largest source of unsteadiness in the blade passage. The same can be said about the evolution of the tip leakage flow, despite its span-wise extent is still not clearly visible from the simulations. As an overall conclusion, CFD determined a good prediction of the global performance and span-wise distribution of flow quantities against experiments, along with a proper description of the averaged

unsteady flow features and corresponding fluctuation amplitudes.

At the present state, further efforts are put to characterize the unsteady nature of the hub corner and tip leakage flows, meanly looking at the characterization of their frequencies. Moreover, as next step, the near-stall condition will be analysed, being this a very critical operating point for the compressor when inlet flow distortions appear.

References

[1] Sebastiampillai J., Rolt A., Nalianda D., Mastropierro F., Sethi V., "Technical and Economic Viability of an EIS 2050 Geared Open Rotor", ASME Turbo Expo GT2019-90290.

[2] Peters A., Spakovszky Z.S., Lord W.K., Rose B., "Ultrashort Nacelles for Low Fan Pressure Ratio Propulsors", Journal of Turbomachinery 137(2) (021001).

[3] Gunn E.J., Hall C.A., "Aerodynamics of Boundary Layer Ingesting Fans", ASME Turbo Expo GT2014-26142 (2014) pp. V01AT01A024.

[4] Giesecke D., Friedrichs J., "Aerodynamic Comparison Between Circumferential and Wing- Embedded Inlet Distortion for an Ultra-High Bypass Ratio Fan Stage", ASME Turbo Expo GT2019-90425.

[5] Perovic D., Hall C.A., Gunn E.J., "Stall Inception in a Boundary Layer Ingesting Fan", ASME Turbo Expo GT2015-43025 (2015) pp. V02AT37A031.

[6] Zhang W., Vahdati M., Stapelfeldt S., "Stall and Recovery Process of a Transonic Fan in Presence of Inlet Distortion", 13th European Turbomachinery Conference ETC2019-371.

[7] Dieck R.H., "Measurement uncertainties - methods and applications", USA: ISA 2007.

[8] Bae J., Kenneth S. B., "Periodic unsteadiness of compressor tip clearance vortex", ASME Turbo Expo GT2004-53015.

[9] Goodhand M. N., Miller R. J., "The impact of real geometries on three-dimensional separations in compressors", ASME Turbo Expo GT2010-22246.

[10] Babin C., Dumas M., Ottavy X., Fontaneto F., "Numerical characterization of a HP compressor stage equipped with a closed shrouded stator cavity", ASME Turbo Expo GT2020-14908.

[11] Roache P.J., "Perspective: A method for uniform reporting of grid refinement studies.", Journal of fluid engineering 116 (3) (1994) : 405–413.

[12] Celik B.I., Ghia U., Roache P.J., freitas C. J., Coleman H., Raas P.E., "Procedure for estimation and reporting of uncertainty due to discretization in CFD applications.", Journal of fluid engineering 130 (078001-1).

[13] Lei V.M., Spakovszky Z.S., Greitzer E.M., "A criterion for axial compressor hub-corner stall", ASME Turbo Expo GT2006-91332.

[14] Taylor J.V., Miller J.M., "Competing three-dimensional machenisms in compressor flows", Journal of turbomachinery 139 (021009-1).

[15] Bennington ;.A., Ross M.H., Cameron J.D., Morris S.C., Du J., Lin F., Cehn J., "An experimental and computational investigation of tip clearance flow and its impact on stall inception.", ASME Turbo Expo GT2010-23516.